



Published in final edited form as:

*Clin Experiment Ophthalmol.* 2015 ; 43(4): 358–366. doi:10.1111/ceo.12299.

## Optical coherence contrast imaging using gold nanorods in living mice eyes

Adam de la Zerda, PhD<sup>1,2</sup>, Shradha Prabhulkar, PhD<sup>3</sup>, Victor L Perez, MD<sup>3</sup>, Marco Ruggeri, PhD<sup>3</sup>, Amit S Paranjape, PhD<sup>3</sup>, Frezghi Habte, PhD<sup>1</sup>, Sanjiv S Gambhir, MD, PhD<sup>1,4,5</sup>, and Richard M Awdeh, MD<sup>3</sup>

<sup>1</sup>Molecular Imaging Program at Stanford, the Bio-X Program and the Department of Radiology, Stanford University, Palo Alto, California

<sup>2</sup>Department of Structural Biology, Stanford University, Palo Alto, California

<sup>3</sup>Bascom Palmer Eye Institute, University of Miami, Miami, Florida, USA

<sup>4</sup>Department of Bioengineering, Stanford University, Palo Alto, California

<sup>5</sup>Department of Materials Science and Engineering, Stanford University, Palo Alto, California

### Abstract

**Background**—Optical coherence tomography (OCT) is a powerful imaging modality to visualize tissue structures, with axial image pixel resolution as high as 1.6  $\mu\text{m}$  in tissue. However, OCT is intrinsically limited to providing structural information as the OCT contrast is produced by optically scattering tissues.

**Methods**—Gold nanorods (GNRs) were injected into the anterior chamber (AC) and cornea of mice eyes which could create a significant OCT signal and hence could be used as a contrast agent for *in vivo* OCT imaging.

**Results**—A dose of 30 nM of GNRs (13 nm in diameter and 45 nm in length) were injected to the AC of mice eyes and produced an OCT contrast nearly 50-fold higher than control mice injected with saline. Furthermore, the lowest detectable concentration of GNRs in living mice AC was experimentally estimated to be as low as 120 pM.

**Conclusions**—The high sensitivity and low toxicity of GNRs brings great promise for OCT to uniquely become a high-resolution molecular imaging modality.

### Keywords

contrast agent; gold nanorods; molecular imaging; ophthalmic imaging; optical coherence tomography

---

**Correspondence:** Dr Richard Awdeh, Bascom Palmer Eye Institute, 900 NW 17<sup>th</sup> Street, Miami, FL 33136, USA. rawdeh@med.miami.edu, Dr Sanjiv Sam Gambhir, Stanford University, 305 Campus Drive, Stanford, CA 94305, USA. sgambhir@stanford.edu, and Dr Adam de la Zerda, Stanford University, 299 Campus Drive, Stanford, CA 94305, USA. adlz@stanford.edu.

*Competing/conflicts of interest:* No stated conflict of interest.

### SUPPORTING INFORMATION

Additional Supporting Information may be found in the online version of this article at the publisher's web-site:

## INTRODUCTION

Optical coherence tomography (OCT) is a noninvasive imaging modality that provides real-time, depth-resolved cross-sectional images of tissue.<sup>1</sup> As the intrinsic contrast of OCT is based on optical scattering, OCT images show primarily structural information, highlighting the boundaries between tissues and tissue layers. Despite not providing physiological or molecular information of tissues, the structural information displayed by OCT is of high value, particularly because it is gained at very high spatial resolution (as low as 1  $\mu\text{m}$ ) and a depth of penetration of several millimetres.<sup>2</sup> This has made OCT a rapidly adopted imaging modality for visualizing pathologies in a wide range of applications ranging from cancer imaging, cardiology<sup>3</sup> and dentistry.<sup>4</sup> The most widespread use of OCT is in ophthalmology. The optics of the eye and the accessibility, namely a clear cornea, make OCT a good candidate for non-contact imaging of the eye.<sup>5</sup> The technology has become a first-line imaging modality for visualizing various diseases of the eye including age-related macular degeneration<sup>6</sup> and diabetic retinopathy,<sup>7</sup> as well as various abnormalities in the eye's anterior segment,<sup>8</sup> including the cornea, the lens and the iris.

Despite the unique imaging properties provided by OCT, its primary limitation is the inability to provide information with respect to the physiology and/or the molecular processes within a tissue of interest. Hence, in order to allow OCT to reach its full potential in providing such information, exogenous contrast agents must be used. This molecular imaging approach has been tested before with numerous imaging modalities including magnetic resonance imaging (MRI), positron emission tomography, fluorescence imaging,<sup>9</sup> Raman spectroscopic imaging,<sup>10</sup> photoacoustic imaging<sup>11</sup> and others.<sup>12</sup> Several contrast agents have been used for the various optical and non-optical imaging modalities, including both small molecules<sup>13</sup> (less than  $\sim 3$  nm), nanoparticles<sup>14</sup> (1–100 nm) and macroscopic particles<sup>15</sup> (larger than 100 nm). However, to date, limited number of contrast agents have been demonstrated for OCT. An OCT contrast agent should exhibit a high optical scattering coefficient, as this reduces the coherency of the probe light beam and increases the OCT contrast. However, this imposes the use of nanoparticles, as molecules below  $\sim 20$  nm in size exhibit negligible optical scattering.<sup>16</sup>

The use of nanoparticles as contrast agents is well established for various imaging modalities including MRI,<sup>17</sup> fluorescence imaging,<sup>18</sup> photoacoustic imaging<sup>19,20</sup> and other modalities.<sup>21</sup> Such contrast agents may be directly administered intravenously for angiographic purposes, as done with other imaging modalities,<sup>22,23</sup> or may be molecularly targeted to proteins of interest.<sup>10–12,24</sup> To allow OCT reach its full potential, highly scattering and biocompatible contrast agents must be designed.

For optical applications, of particular interest are gold-based nanoparticles, as they display a strong plasmonic resonance for interaction with light.<sup>16</sup> In particular, rod-shaped gold nanostructures exhibit a red-shifted plasmonic resonance, whose peak wavelength depends primarily on the aspect ratio of the rod. As the aspect ratio of the gold nanorod (GNR) increases, the resonance peak wavelengths increases from 530 nm up to 1000 nm or more.<sup>25</sup> This shift of the peak resonance towards near infrared (NIR) wavelengths allows for deeper tissue penetration.<sup>26</sup>

Although several OCT contrast agents has been previously proposed,<sup>27–29</sup> none that we know of has been shown to demonstrate a detectable signal in living tissues. In this work, we leverage recent advancements in the synthesis of GNRs with peak resonance at the NIR and demonstrate their use as contrast agents for OCT.

## METHODS

### GNR preparation

GNRs with an absorbance peak at 780 nm and 850 nm were used in this study (Nanopartz, Loveland, CO, USA). To prevent the raw GNRs from aggregating, the particles were suspended in cetyltrimethylammonium bromide (CTAB) by the manufacturer, which is potentially toxic for *in vivo* use. To make the GNRs more biologically compatible, we removed the CTAB and coated the GNRs with polyethylene glycol to render water solubility and to minimize potential toxicity effects. We have used thiol-terminated polyethylene glycol (PEG) to displace the cytotoxic CTAB from the surface of the GNRs. The presence of PEG introduces *in vivo* stealth characteristics to the GNRs. PEG forms a water-like layer on the surface of the GNRs, making them less visible to CD45+ leukocytes and subsets (T cells, myeloid cells, macrophages, neutrophils). This is done by taking 50 mL of 1.5 nM raw GNRs suspended in CTAB and centrifuged three times (5000 r.p.m. for 5 min, followed by 7000 r.p.m. for 20 min, followed by 9000 r.p.m. for 20 min). After each centrifugation step, the supernatant was removed and the GNRs were suspended in 4 mL of DI water. We then incubated the GNRs in 1 mL of 5.4 mM PEG (HS-PEG<sub>5000</sub>-COOH) and incubated the solution for 96 h. The CTAB on the GNRs was replaced by thiol groups present on the HS-PEG<sub>5000</sub>-COOH polymer using a process known as ligand exchange. Ligand exchange allows for the removal and replacement of CTAB from the surface of the GNRs in a controlled manner, thus preventing particle aggregation and allowing the particles to retain their size, shape and plasmon resonant characteristics.<sup>30,31</sup>

### Optical and electron microscopy characterization of the GNR

The GNR optical absorbance spectrum and extinction coefficient were calculated using the DU-640 spectrophotometer (Beckman Coulter, Brea, CA, USA). The final concentration of the particles after centrifugation and washes was calculated.

The transmission electron microscopy (TEM) analysis of the GNRs was done using a CM10 transmission electron microscope (Philips, Amsterdam, Netherlands) operating at 80 kV. Analysis of distribution of particle sizes was done through calculating the sizes of 35 random GNRs in the TEM images using ImageJ National Institutes of Health (NIH).

### Phantom studies

Two different sizes of GNRs were tested to measure their back-scattering properties based on the intensity of OCT signal. GNRs corresponding to a peak absorbance wavelength of 780 nm (length =  $43 \pm 4.22$  nm; axial diameter =  $12 \pm 0.25$  nm) and 850 nm (length =  $49.31 \pm 6.9$  nm; axial diameter =  $12.09 \pm 1.63$  nm) were serially diluted and placed in 96-well plates. Four readings were conducted for each concentration of GNR solution. OCT image of each well was separately recorded using the 1-inch telecentric lens with the following

parameters: 2-mm lateral scan size, 200 A-lines per OCT B-scan, 1 B-scan and 1000 frames per B-scan.

### Animal injection

All animal experiments were performed in compliance with the University of Miami Institutional Animal Care and Use Committee (IACUC) Guidelines. Wild-type C57BL/6 mice, age 9–16 months and weighing 25–30 g, were utilized for the study. The mice eyes were dilated using a 2.5% phenylephrine hydrochloride ophthalmic solution 10 min prior to administration of anaesthesia. The mice were anaesthetized through a peritoneal injection of (100  $\mu$ L/20 mg) solution containing ketamine (1.5 mg/0.1 mL) and xylazine (0.3 mg/0.1 mL) in sterile PBS. Corneal and AC injections were carried out after the animal was under anaesthesia. We standardized an AC injection technique which involved initially puncturing the AC to drain out fluid, then a 33-gauge blunt needle was inserted into the same opening and 3–5  $\mu$ L of GNR solution was injected. We standardized a corneal injection where a linear superficial incision was created at the limbus of the mouse cornea, a stromal tunnel was created from the limbus to the central corneal stroma, and 5–10  $\mu$ L of solution was injected using a 33-gauge blunt needle. OCT imaging was performed immediately after the corneal and AC injections were performed with the animal still under anaesthesia. The animals were placed in a custom-built holder which provided precise and reproducible alignment of the animals for OCT imaging.

To evaluate the OCT signal produced by GNR in living tissues, we first standardized a GNR-850 AC injection technique where 3–5  $\mu$ L of solution was injected into the mice AC. GNR-850 diluted using matrigel were injected at concentrations of 30 nM, 7.5 nM, 1.9 nM, 0.5 nM, 120 pM and 29 pM to evaluate the potential of GNR-850 as OCT contrast agents in living subjects. Matrigel, which does not have any inherent scattering capability, was used to localize the GNR-850 in the AC and prevent losses of GNR-850 due to leaking. Additionally, a naïve group of mice corneas not receiving injections was included ( $N = 2$  mice). Upon injection, mice AC were scanned using Bioptigen SDOIS spectral domain OCT instrument (Bioptigen, Durham, NC).<sup>32</sup> The power of the sample arm illuminating the tissue was set to 720  $\mu$ W, which is well within the American National Standards Institute limits.<sup>33</sup>

We then tested the applicability of GNR-780 as an OCT contrast agent by injecting 5–10  $\mu$ L of GNR-780 at a concentration of 50 nM into the stroma of a mouse cornea. A control group of mice received intrastromal injection of balanced salt solution (BSS) into their corneas using the same injection technique. Additionally, a naïve group of mice corneas not receiving injections was included ( $N = 3$  mice).

Finally, we aimed to assess the minimal detectable concentration of GNR-780 in living mice corneas. Using the same corneal injection technique, we injected mice corneas ( $N = 4$  mice for four concentrations) with 5  $\mu$ L of GNRs at decreasing concentrations ranging from 50 nM to 0.05 nM.

We then created a three-dimensional (3D) rendering of the OCT image, as well as a rotating video of the 3D rendering (Supporting Information Video S1) using the commercial software Amira 5.3 (Visage Imaging San Diego, CA, USA). The 3D rendering visualizes

well the various anatomical structures of the cornea and highlights the GNR contrast in the cornea.

### Ultrahigh temporal and spatial resolution spectral domain OCT system

Commercially available Spectral Domain Ophthalmic Imaging System (SDOIS) from Biophtigen, Inc. was used for imaging the anterior segment of the mouse eye, using a 860 nm centre wavelength super luminescent diode with a bandwidth of 95 nm.

### Displaying and thresholding of OCT images

The maximum value for the colour scale was normalized such that the average OCT signal in an area in the AC that was not injected with GNR was equal across all images. This slight adjustment was needed so as to normalize for changes in absolute OCT signal in AC positioned physically closer to the telecentric lens of the OCT camera. The new colour scale with adjusted maximum value was therefore called OCT contrast (as opposed to OCT signal). These adjustments in maximum scale level were relatively small and did not exceed  $\pm 13\%$  at most. Furthermore, the OCT images displayed in this work exhibited some intrinsic and homogeneous noise. Therefore, the minimum value of the colour scale for displaying the images was selected to be 1.5 times the average noise in the background of the image.

### Statistical analysis

Statistical analysis of difference between two groups had been done using the two-sided student's *t*-test.

## RESULTS

GNRs possess strong optical absorbance and scattering properties when illuminated by an incident light.<sup>25</sup> In this work we demonstrate, that the strong optical scattering produced by GNRs can be used to create an OCT signal stronger than the background signal of some tissues in the eye. We demonstrate the utility of GNRs as OCT contrast agents in living animals and show that they produce strong signal in the eyes of living mice. To determine the optimal peak wavelength of GNRs for enhanced OCT contrast generation, two different sizes of GNRs were evaluated using a phantom setup. OCT images obtained from GNRs corresponding to peak absorbance wavelengths of 780 nm (GNR-780) and 850 nm (GNR-850), respectively, are shown in (Fig. 1a,b). The OCT signal produced by GNR-850 was consistently higher than the signal produced by GNR-780 (Fig. 1c). The lowest detectable concentration for GNR-850 and GNR-780 is 230 pM and 750 pM, respectively. This is likely due to the greater overlap of the GNR-850 absorbance spectrum and the light source used in the spectral domain OCT system ( $860 \pm 48$  nm). This overlap causes collective, in-phase oscillations of conductive electrons at the surface of the GNRs known as localized surface plasmon resonance (LSPR) effect. The LSPR effect results in maxima of light scattering and absorption at the surface of the GNRs.<sup>30</sup> An important advantage of GNR-850 and GNR-780 is the fact that they minimally overlap with other major endogenous absorbers such as oxygenated and deoxygenated hemoglobin (Fig. 2a). Finally, we characterized the diameter and length of the GNR-850 and their distribution using TEM (Fig. 2b,c). The GNR-850 were  $12.09 \pm 1.63$  nm in diameter and  $49.31 \pm 6.9$  nm in length

(average  $\pm$  standard deviation [SD]). The GNR-780 were  $12 \pm 0.25$  nm in diameter and  $43 \pm 4.22$  nm in length (average  $\pm$  SD).

GNR-850 (29 pM) injected into the AC did not produce distinct contrast as compared with the background/matrigel (0 pM) injected AC ( $P < 0.23$ , two-sided student's *t*-test), concentrations of 120 pM and higher produced significantly different OCT contrast (Fig. 3a) ( $P < 0.05$ , for any one of the groups). We used a region-of-interest (ROI) analysis to compute the difference in OCT signal from the AC of naïve, matrigel-injected and GNR-850-injected mice. Figure 3b shows the log–log plot of GNR-850 concentration plotted *versus* the normalized OCT intensities converted to contrast OCT and calculated using ROI analysis.

*In vivo* high-resolution OCT images of the mice corneas revealed a high OCT contrast in the cornea injected with GNR-780 as compared with the control corneas (Fig. 4). Although BSS alone produced no OCT signal (data not shown), eyes injected with BSS showed minimal OCT signal, likely due to the injection itself, which may have altered and slightly moved tissues in the cornea. We used an ROI analysis to compute the difference in OCT signal from the cornea of naïve, BSS-injected and GNR-780-injected mice. We found that the OCT signal from corneas injected with nanoparticles was three times higher than OCT signal from BSS-injected mice corneas and 7.5 times higher than OCT signal from naïve mice corneas. A minimum threshold of 1.5 times the OCT noise was applied to the images for better clarity and visibility of features.

We next aimed to quantify the lowest detectable concentration of GNR-780 in a mouse cornea by injecting GNR-780 at varying concentrations to the mice corneas. Although the lowest concentration of 0.05 nM produced an indistinguishable OCT contrast compared with control mice, mice injected with 0.5 nM produced a clear OCT contrast, slightly higher than the control mice. Concentrations of 5 nM and higher produced an even greater OCT contrast (Fig. 5b). Some mice have experienced slight thickening of the cornea because of the volume (5  $\mu$ L) of the injection. However, all corneas returned to normal thickness of  $\sim 130$   $\mu$ m by 48 h post-injection (data not shown).

The 3D OCT images were then quantitatively analysed by manually drawing ROI encapsulating the injection area in the cornea and calculating the average signal within this 3D ROI (Fig. 5c). The analysis has confirmed the qualitative observation that mice injected with 0.05 nM were indistinguishable from control mice ( $P < 0.23$ , two-sided student's *t*-test), and all other injections gave an OCT contrast that was significantly higher than control mice signal ( $P < 0.05$  for any one of the groups). As 0.5 nM concentration of GNR produced a signal 33% higher than control mice injected with BSS alone, it was extrapolated that about 0.37 nM of GNR is the *in vivo* sensitivity limit (i.e. the concentration where the signal to tissue background ratio equals to 1). As the endogenous OCT signal produced by the cornea was over 500% higher than the OCT instrument noise floor ( $P < 0.01$ ), the sensitivity is hence limited by the endogenous tissue background signal.

We have characterized and demonstrated the application of GNRs as high-sensitivity contrast agents for OCT in living animals. The sensitivity limit in living mice corneas was



estimated to be 120 pM, comparable with the sensitivity limit of *in vivo* fluorescence imaging using comparable size and wavelength fluorescent nanoparticles.<sup>34</sup> However, the fact that OCT imaging of GNRs can maintain such high sensitivity is particularly powerful as the images produced are at ultrahigh spatial resolution (3  $\mu$ m).

## DISCUSSION

OCT is currently one of the leading diagnostic tools in ophthalmology, as it allows for non-invasive, ultrahigh spatial resolution structural imaging of tissue morphology. In addition to ophthalmology, OCT has found broad range of applications as an *in vivo* cellular imaging technique for cardiology,<sup>35</sup> dermatology,<sup>36</sup> neurology<sup>37</sup> and oncology.<sup>38</sup> However, OCT is still currently limited in visualizing physiological and molecular features, as the mechanism of contrast is purely the optical scattering of tissues.

The field of ophthalmology has seen the most rapid adoption of OCT as a diagnostic device. The optically clear gel inside the eyeball as well as the optics of the eye lens makes the eye amenable for easy investigation using non-contact optical techniques. Apart from OCT, currently available clinical ophthalmic imaging instruments are primarily light-based and include: fundus photography, scanning laser ophthalmoscopy,<sup>39</sup> fluorescein angiography<sup>40</sup> and indocyanine green angiography.<sup>23</sup> Ophthalmic ultrasound devices<sup>41</sup> are also used in the case of poor optical visualization such as in the case of haemorrhages or ocular tumours. However, all these imaging devices are limited in their ability to provide mostly morphological information about the eye structure and limited functional information. Therefore, disease detection and treatment monitoring is intrinsically limited to late-stage anatomic and vascular abnormalities. Moreover, these techniques cannot visualize the underlying molecular and physiological causes of a disease. Emerging OCT-based imaging modalities, such as magnetomotive OCT,<sup>29</sup> show promise in providing molecular information through the use of contrast agents; however, these modalities require the use of an external coil and a large radiofrequency amplifier, which complicates the system significantly.

In contrast, by conjugating the GNRs described here to targeting moieties such as antibodies<sup>42</sup> or peptides,<sup>43</sup> one will likely be able to target the GNRs to disease-associated molecular targets<sup>12</sup> and visualize them with OCT. A great benefit of using gold-based nanoparticles is the potential for lower cytotoxicity because of the inert properties of gold.<sup>44,45</sup> Finally, another unique advantage of GNRs is that their peak absorbance may be tuned from 600 nm up to and over 1000 nm by altering the particle's aspect ratio.<sup>46</sup> Furthermore, although the route of administration selected here was a local injection to the eye, future avenues would explore systemic administration alternatives, which may prove useful for specific cases where fast clearance rates are needed or when the molecular target of interest is vascular. It is likely that the clearance path of the GNR from the cornea is through the vasculature and lymphatic system at the corneal limbus. However, further studies would have to address this question separately. Finally, although GNRs were used in the current work, other agents, including other types of metallic and non-metallic nanoparticles, may eventually be useful as well.

In order to visualize the GNRs in an OCT image, the OCT signal (light scattering) from the GNRs must exceed the OCT signal from the surrounding tissue. As different parts of the eye exhibit different background OCT signals, the sensitivity limit will change accordingly. Additionally, in the future, changing the OCT excitation light source to cover different wavelengths may further improve the sensitivity, as different parts of the eye have different absorbance spectra.<sup>47</sup>

We believe OCT molecular imaging using GNRs bears great promise to fundamentally change the way ophthalmic diseases are diagnosed today. Although this work primarily explores application in ophthalmology, the underlying physical principles of contrast enhancement are extendible to other areas such as cardiology<sup>35</sup> and cancer imaging.<sup>38</sup> This work provides an additional benefit that we did not need to modify the OCT instrumentation (such as in case of magnetomotive<sup>48</sup> or photothermal OCT<sup>49</sup>). We anticipate that this work may also open opportunities for targeted molecular imaging agents in other non-ophthalmic OCT applications.

## Supplementary Material

Refer to Web version on PubMed Central for supplementary material.

## Acknowledgments

National Institute of Health – NEI R21EY020940 (RMA), NCI CCNE U54 CA119367 (SSG), NCI ICMIC P50 CA114747 (SSG), DP5 0D012179 (AD), U.S. Army Medical Research and Material Command W81XWH-09-1-0025 as Department of Defense Breast Cancer Research Program Predoctoral Traineeship Award (AD), the Canary Foundation (SSG), the Bio-X Program at Stanford – Graduate Student Fellowship (AD), The Wallace H. Coulter Center for translational research (RMA), Bio-X Interdisciplinary Initiatives Program IIP6-43 (AD), and the Arnold and Mabel Beckman Initiative for Macular Research 1407 (AD), and the United States Air Force FA9550-15-1-0007 (AD). The authors would also like to thank Jim Strommer (Stanford University) for helping with figure graphics and Dr Jay Wang (University of Miami) for access to his optical coherence tomography laboratory, as well as descriptive information related to optical coherence tomography hardware.

## References

1. Huang D, Swanson EA, Lin CP, et al. Optical coherence tomography. *Science*. 1991; 254:1178–81. [PubMed: 1957169]
2. Drexler W, Morgner U, Kurtner FX, et al. In vivo ultrahigh-resolution optical coherence tomography. *Opt Lett*. 1999; 24:1221–3. [PubMed: 18073990]
3. Jang IK, Bouma BE, Kang DH, et al. Visualization of coronary atherosclerotic plaques in patients using optical coherence tomography: comparison with intravascular ultrasound. *J Am Coll Cardiol*. 2002; 39:604–9. [PubMed: 11849858]
4. Otis LL, Everett MJ, Sathyam US, Colston BW Jr. Optical coherence tomography: a new imaging technology for dentistry. *J Am Dent Assoc*. 2000; 131:511–14. [PubMed: 10770016]
5. de la Zerda A, Kim J-W, Galanzha EI, Gambhir SS, Zharov VP. Advanced contrast nanoagents for photoacoustic molecular imaging, cytometry, blood test and photothermal theranostics. *Contrast Media Mol Imaging*. 2011; 6:346–69. [PubMed: 22025336]
6. Puliafito CA, Hee MR, Lin CP, et al. Imaging of macular diseases with optical coherence tomography. *Ophthalmology*. 1995; 102:217–29. [PubMed: 7862410]
7. Hee MR, Puliafito CA, Duker JS, et al. Topography of diabetic macular edema with optical coherence tomography. *Ophthalmology*. 1998; 105:360–70. [PubMed: 9479300]
8. Hirano K, Ito Y, Suzuki T, Kojima T, Kachi S, Miyake Y. Optical coherence tomography for the noninvasive evaluation of the cornea. *Cornea*. 2001; 20:281–9. [PubMed: 11322417]



9. Ntziachristos V, Razansky D. Molecular imaging by means of multispectral optoacoustic tomography (MSOT). *Chem Rev.* 2010; 110:2783–94. [PubMed: 20387910]
10. Keren S, Zavaleta C, Cheng Z, de la Zerda A, Gheysens O, Gambhir SS. Noninvasive molecular imaging of small living subjects using Raman spectroscopy. *Proc Natl Acad Sci U S A.* 2008; 105:5844–9. [PubMed: 18378895]
11. de la Zerda A, Zavaleta C, Keren S, et al. Carbon nanotubes as photoacoustic molecular imaging agents in living mice. *Nat Nanotechnol.* 2008; 3:557–62. [PubMed: 18772918]
12. Massoud TF, Gambhir SS. Molecular imaging in living subjects: seeing fundamental biological processes in a new light. *Genes Dev.* 2003; 17:545–80. [PubMed: 12629038]
13. Frangioni JV. In vivo near-infrared fluorescence imaging. *Curr Opin Chem Biol.* 2003; 7:626–34. [PubMed: 14580568]
14. Weissleder R, Kelly K, Sun EY, Shtatland T, Josephson L. Cell-specific targeting of nanoparticles by multivalent attachment of small molecules. *Nat Biotechnol.* 2005; 23:1418–23. [PubMed: 16244656]
15. Blomley MJK, Cooke JC, Unger EC, Monaghan MJ, Cosgrove DO. Microbubble contrast agents: a new era in ultrasound. *BMJ.* 2001; 322:1222–5. [PubMed: 11358777]
16. Jain PK, Lee KS, El-Sayed IH, El-Sayed MA. Calculated absorption and scattering properties of gold nanoparticles of different size, shape, and composition: applications in biological imaging and biomedicine. *J Phys Chem B.* 2006; 110:7238–48. [PubMed: 16599493]
17. Mulder WJM, Strijkers GJ, Habets JW, et al. MR molecular imaging and fluorescence microscopy for identification of activated tumor endothelium using a bimodal lipidic nanoparticle. *FASEB J.* 2005; 19:2008–10. [PubMed: 16204353]
18. Rao J, Dragulescu-Andrasi A, Yao H. Fluorescence imaging in vivo: recent advances. *Curr Opin Biotechnol.* 2007; 18:17–25. [PubMed: 17234399]
19. Yang X, Stein EW, Ashkenazi S, Wang LV. Nanoparticles for photoacoustic imaging. *Wiley Interdiscip Rev Nanomed Nanobiotechnol.* 2009; 1:360–8. [PubMed: 20049803]
20. de la Zerda A, Kim J-W, Galanzha EI, Gambhir SS, Zharov VP. Carbon nanotube-based photoacoustic and photothermal contrast agents. *Contrast Media Mol Imaging.* 2011; 6:346–69. [PubMed: 22025336]
21. Sanvicens N, Marco MP. Multifunctional nanoparticles – properties and prospects for their use in human medicine. *Trends Biotechnol.* 2008; 26:425–33. [PubMed: 18514941]
22. Caravan P, Ellison JJ, McMurry TJ, Lauffer RB. Gadolinium(III) chelates as MRI contrast agents: structure, dynamics, and applications. *Chem Rev.* 1999; 99:2293–352. [PubMed: 11749483]
23. Stanga PE, Lim JI, Hamilton P. Indocyanine green angiography in chorioretinal diseases: indications and interpretation: an evidence-based update. *Ophthalmology.* 2003; 110:15–21. quiz 2–3. [PubMed: 12511340]
24. Willmann JK, Paulmurugan R, Chen K, et al. US imaging of tumor angiogenesis with microbubbles targeted to vascular endothelial growth factor receptor type 2 in mice. *Radiology.* 2008; 246:508–18. [PubMed: 18180339]
25. Link S, Mohamed MB, El-Sayed MA. Simulation of the optical absorption spectra of gold nanorods as a function of their aspect ratio and the effect of the medium dielectric constant. *J Phys Chem B.* 1999; 103:3073–7.
26. Wang L, Jacques SL, Zheng L. MCML – Monte Carlo modeling of light transport in multi-layered tissues. *Comput Methods Programs Biomed.* 1995; 47:131–46. [PubMed: 7587160]
27. Zysk AM, Nguyen FT, Oldenburg AL, Marks DL, Boppart SA. Optical coherence tomography: a review of clinical development from bench to bedside. *J Biomed Opt.* 2007; 12:051403. [PubMed: 17994864]
28. Chen J, Saeki F, Wiley BJ, et al. Gold nanocages: bioconjugation and their potential use as optical imaging contrast agents. *Nano Lett.* 2005; 5:473–7. [PubMed: 15755097]
29. Oldenburg A, Toublan F, Suslick K, Wei A, Boppart S. Magnetomotive contrast for in vivo optical coherence tomography. *Opt Express.* 2005; 13:6597–614. [PubMed: 19498675]
30. Wijaya A, Hamad-Schifferli K. Ligand customization and DNA functionalization of gold nanorods via round-trip phase transfer ligand exchange. *Langmuir.* 2008; 24:9966–9. [PubMed: 18717601]

31. Grabinski C, Schaeublin N, Wijaya A, et al. Effect of gold nanorod surface chemistry on cellular response. *ACs Nano*. 2011; 5:2870–9. [PubMed: 21405102]
32. Ruggeri M, Wehbe H, Jiao S, et al. In vivo three-dimensional high-resolution imaging of rodent retina with spectral-domain optical coherence tomography. *Invest Ophthalmol Vis Sci*. 2007; 48:1808–14. [PubMed: 17389515]
33. American National Standards Institute. American National Standard for the Safe Use of Lasers, ANSI Standard Z1361-2000. New York: ANSI, Inc; 2000.
34. de la Zerda A, Bodapati S, Teed R, et al. A comparison between time domain and spectral imaging systems for imaging quantum dots in small living animals. *Mol Imaging Biol*. 2010; 12:500–8. [PubMed: 20012220]
35. Villard J, Paranjape A, Victor D, Feldman M. Applications of optical coherence tomography in cardiovascular medicine, Part 2. *J Nucl Cardiol*. 2009; 16:620–39. [PubMed: 19479314]
36. Welzel J. Optical coherence tomography in dermatology: a review. *Skin Res Technol*. 2001; 7:1–9. [PubMed: 11301634]
37. Boppart SA, Bouma BE, Brezinski ME, Tearney GJ, Fujimoto JG. Imaging developing neural morphology using optical coherence tomography. *J Neurosci Methods*. 1996; 70:65–72. [PubMed: 8982983]
38. Loo C, Lowery A, Halas N, West J, Drezek R. Immunotargeted nanoshells for integrated cancer imaging and therapy. *Nano Lett*. 2005; 5:709–11. [PubMed: 15826113]
39. Sharp PF, Manivannan A, Xu H, Forrester JV. The scanning laser ophthalmoscope – a review of its role in bioscience and medicine. *Phys Med Biol*. 2004; 49:1085–96. [PubMed: 15128191]
40. Kang SW, Park CY, Ham DI. The correlation between fluorescein angiographic and optical coherence tomographic features in clinically significant diabetic macular edema. *Am J Ophthalmol*. 2004; 137:313–22. [PubMed: 14962423]
41. Silverman RH. High-resolution ultrasound imaging of the eye – a review. *Clin Experiment Ophthalmol*. 2009; 37:54–67. [PubMed: 19138310]
42. Eghtedari M, Liopo AV, Copland JA, Oraevsky AA, Motamedi M. Engineering of hetero-functional gold nanorods for the in vivo molecular targeting of breast cancer cells. *Nano Lett*. 2009; 9:287–91. [PubMed: 19072129]
43. Li Z, Huang P, Zhang X, et al. RGD-conjugated dendrimer-modified gold nanorods for in vivo tumor targeting and photothermal therapy. *Mol Pharm*. 2010; 7:94–104. [PubMed: 19891496]
44. Hauck TS, Ghazani AA, Chan WC. Assessing the effect of surface chemistry on gold nanorod uptake, toxicity, and gene expression in mammalian cells. *Small*. 2008; 4:153–9. [PubMed: 18081130]
45. Connor EE, Mwamuka J, Gole A, Murphy CJ, Wyatt MD. Gold nanoparticles are taken up by human cells but do not cause acute cytotoxicity. *Small*. 2005; 1:325–7. [PubMed: 17193451]
46. Yu Y-Y, Chang S-S, Lee C-L, Wang CRC. Gold nanorods: electrochemical synthesis and optical properties. *J Phys Chem B*. 1997; 101:6661–4.
47. Hammer M, Roggan A, Schweitzer D, Muller G. Optical properties of ocular fundus tissues – an in vitro study using the double-integrating-sphere technique and inverse Monte Carlo simulation. *Phys Med Biol*. 1995; 40:963–78. [PubMed: 7659735]
48. Oldenburg AL, Crecea V, Rinne SA, Boppart SA. Phase-resolved magnetomotive OCT for imaging nanomolar concentrations of magnetic nanoparticles in tissues. *Opt Express*. 2008; 16:11525–39. [PubMed: 18648474]
49. Paranjape AS, Kuranov R, Baranov S, et al. Depth resolved photothermal OCT detection of macrophages in tissue using nanorose. *Biomed Opt Express*. 2010; 1:2–16. [PubMed: 21258441]

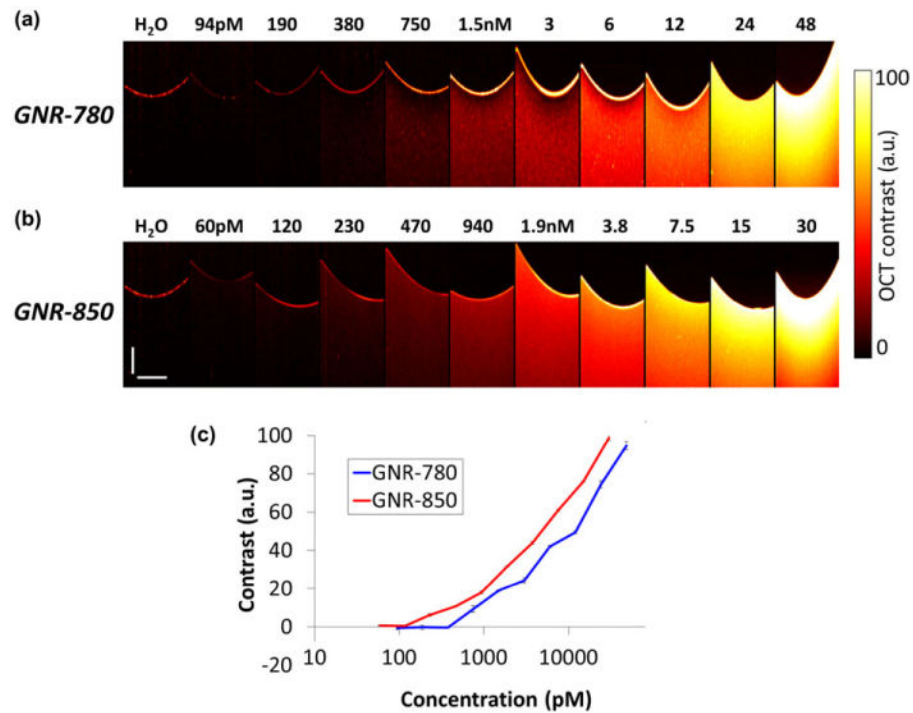


**Figure 1.**

Gold nanorod (GNR) optical coherence tomography (OCT) phantom studies. (a) OCT images recorded of wells containing GNRs dissolved in D.I. water corresponding to peak extinction wavelength of 780 nm at increasing concentrations from 0 to 48 nM. (b) OCT images recorded of wells containing GNRs dissolved in D.I. water corresponding to peak extinction wavelength of 850 nm at increasing concentrations from 0 to 30 nM. (c) Graph depicting OCT contrast generated by GNRs *versus* concentration of GNRs present in each corresponding well. GNRs with an extinction peak at 850 nm display higher OCT contrast as compared with 780 nm GNRs for each of the concentrations tested.

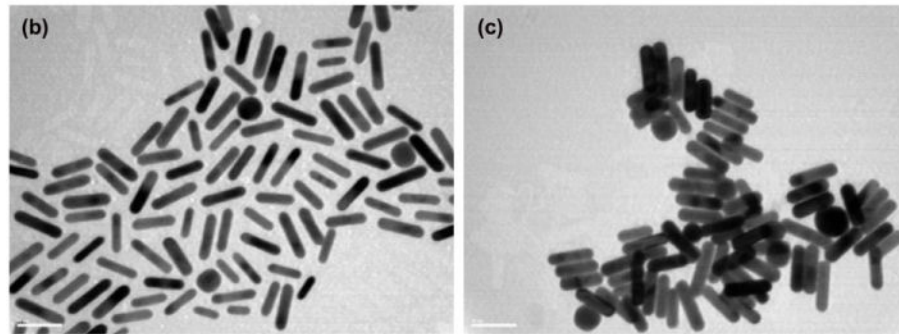
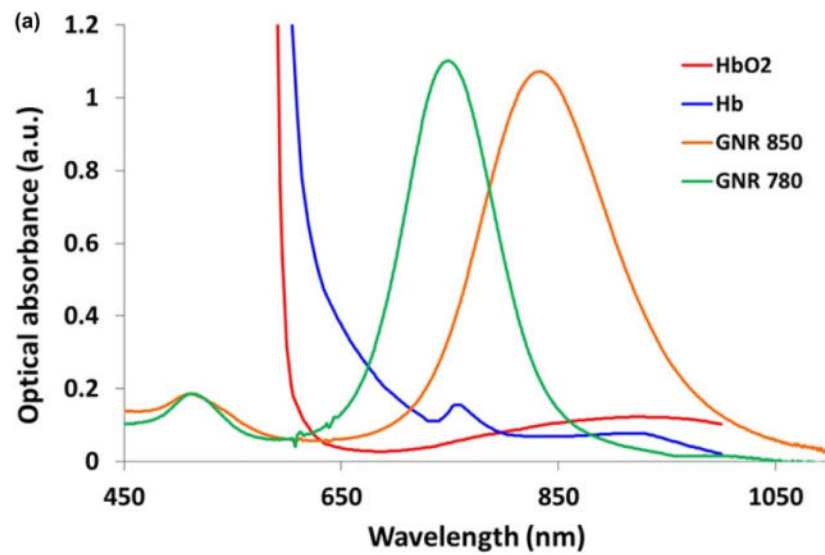


**Figure 2.**

*In vitro* characterization of the gold nanorods (GNRs). (a) The optical absorbance spectrum of GNR-780 (green curve) and GNR-850 (orange curve) peaked at 780 nm and 850 nm, respectively. These are preferable wavelengths as the optical absorbance of oxygenated (red curve) and deoxygenated hemoglobin (blue curve) are minimal at these wavelengths. (b) Transmission electron microscopy image of the 850 nm GNR (length =  $49.31 \pm 6.9$  nm; axial diameter =  $12.09 \pm 1.63$  nm). (c) Transmission electron microscopy image of the 780 nm GNR (length =  $43 \pm 4.22$  nm; axial diameter =  $12 \pm 0.25$  nm).

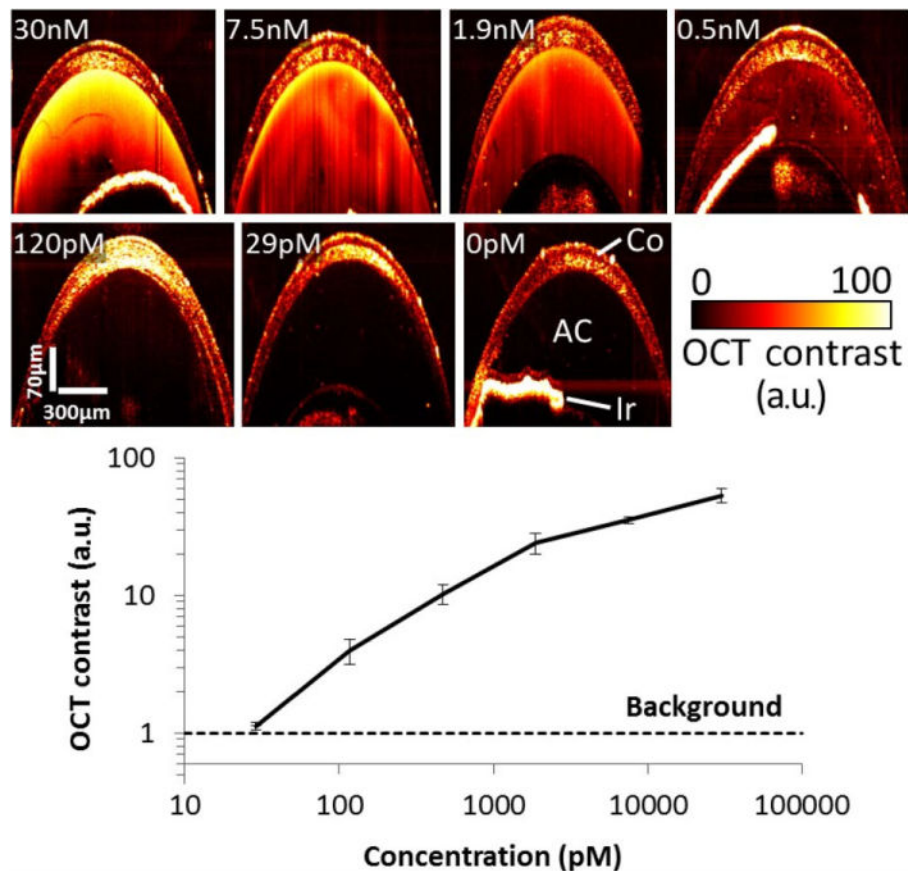


**Figure 3.**

Quantifying gold nanorod (GNR) detection limit in the anterior chamber (AC) *in vivo*. (a) Mice ACs were injected with 3–5  $\mu\text{L}$  of GNR-850 nanoparticles at decreasing concentrations from 30 nM to 0 nM ( $N = 12$  total mice). Control mice ACs were injected with Matrigel. Although mice injected with 29 pM of GNR-850 solution displayed contrast similar to control mice, concentrations of 120 pM and above produced a distinct detectable OCT signal. (b) Quantification of the OCT contrast (measured as signal from area of injection divided by signal from an area distant from the injection) was observed to increase with the GNR concentration, with the lowest detectable concentration being 120 pM. Below this concentration, the OCT contrast was about equal to the OCT contrast recorded from the control mice (denoted as *Background* in black dashed line). The error bars represent standard deviation of the OCT signal.

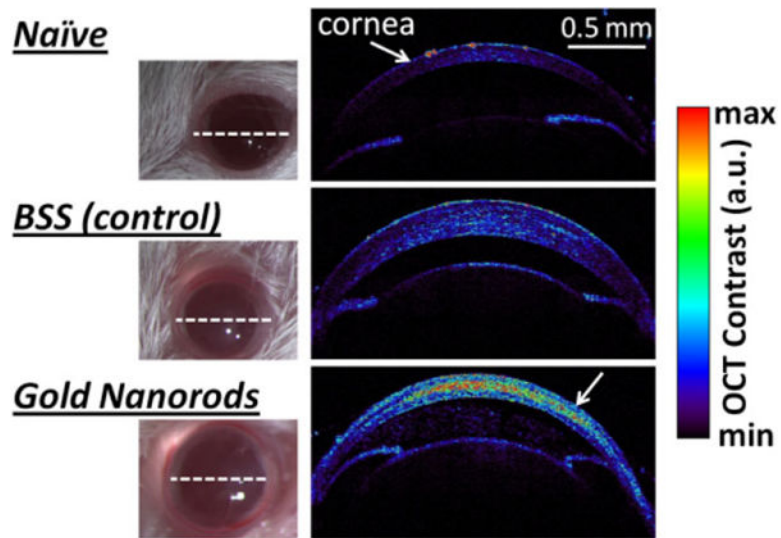


**Figure 4.**

OCT detection of GNR-780 in living mice corneas. Mice corneas were injected with 10  $\mu$ L of GNR-780 at 50 nM (lower mouse), and control mice corneas were injected with 10  $\mu$ L of balanced saline solution (middle mouse) or not injected at all (upper mouse). OCT cross-sectional images through the mice eyes (white dotted line) visualized the high contrast created by the GNR-780 in the cornea (lower white arrow) as compared with control mice.



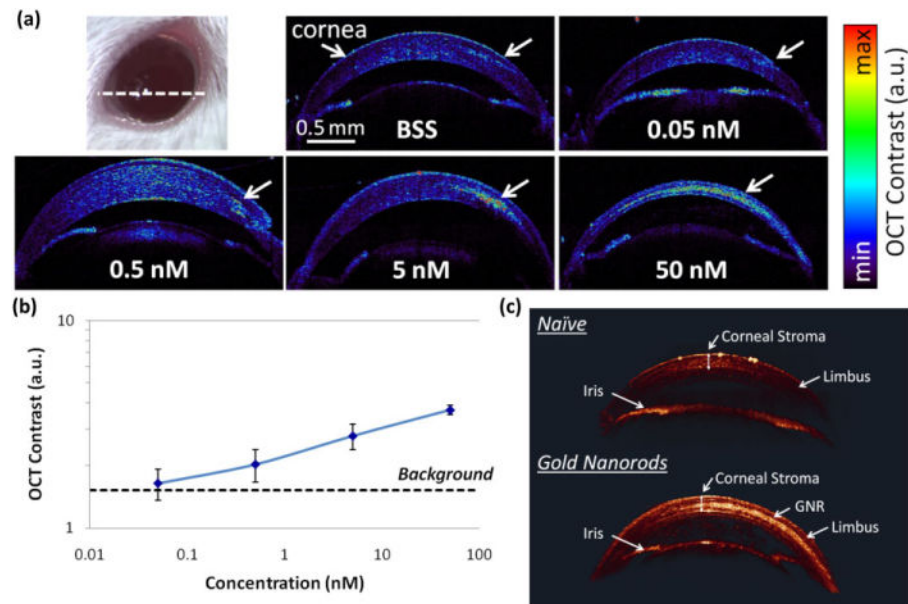


**Figure 5.**

Quantifying GNR detection limit in mouse cornea. (a) Mice corneas were injected with 5  $\mu\text{L}$  of GNR nanoparticles at decreasing concentrations from 50 nM to 0.05 nM ( $N = 4$  total mice), and control mice corneas were injected with balanced saline solution (BSS).

Although mice injected with 0.05 nM exhibited OCT contrast similar to control mice, concentrations of 0.5 nM and above produced a distinct detectable OCT signal. The OCT images represent a cross-sectional slide through the cornea (white dashed line). (b)

Quantification of the OCT contrast (measured as signal from area of injection divided by corneal signal from an area distant from the injection) was observed to increase with the GNR concentration, with the lowest detectable concentration being 0.5 nM. Below this concentration, the OCT contrast was about equal to the OCT contrast recorded from the control mouse that was injected with BSS (denoted as *Background* in black dashed line). The error bars represent standard deviation of the OCT signal. (c) 3D rendering of OCT image. Although naïve mice show minimal signal in the corneal stroma (upper eye), mice injected with 10  $\mu\text{L}$  of GNR at 50 nM show a bright and distinct OCT signal from the corneal stroma (lower eye). The corneal structures (corneal stroma, limbus and iris) exhibit very consistent OCT signal intensities across both the naïve and injected eyes. For 3D rotating videos, see Supporting Information videos.